Fracture toughness and crack resistance curves for fiber compressive failure mode in polymer composites under high rate loading

Kuhn, P., Catalanotti, G., Xavier, J., Camanho, P. P., & Koerber, H. (2017). Fracture toughness and crack resistance curves for fiber compressive failure mode in polymer composites under high rate loading. *Composite Structures*, *182*, 164-175. https://doi.org/10.1016/j.compstruct.2017.09.040

Published in:
Composite Structures

Document Version:
Peer reviewed version

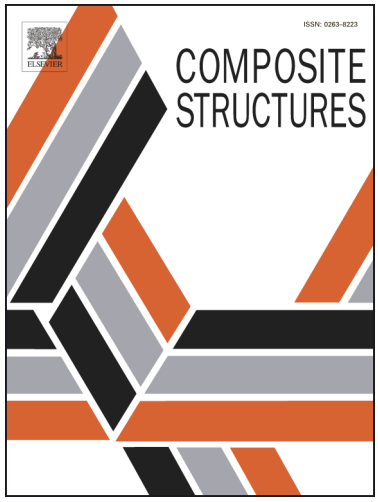

Fracture toughness and crack resistance curves for fiber compressive failure mode in polymer composites under high rate loading

P. Kuhn, G. Catalanotti, J. Xavier, P.P. Camanho, H. Koerber

PII: S0263-8223(17)32082-2
DOI: http://dx.doi.org/10.1016/j.compstruct.2017.09.040
Reference: COST 8903

To appear in: *Composite Structures*

Received Date: 6 July 2017
Revised Date: 15 September 2017
Accepted Date: 16 September 2017

Please cite this article as: Kuhn, P., Catalanotti, G., Xavier, J., Camanho, P.P., Koerber, H., Fracture toughness and crack resistance curves for fiber compressive failure mode in polymer composites under high rate loading, *Composite Structures* (2017), doi: http://dx.doi.org/10.1016/j.compstruct.2017.09.040

Fracture toughness and crack resistance curves for fiber compressive failure mode in polymer composites under high rate loading

P. Kuhn[a,*], G. Catalanotti[b], J. Xavier[c,d], P.P. Camanho[c,e], H. Koerber[a]

[a] *Technical University of Munich, Department of Mechanical Engineering, Chair for Carbon Composites, Boltzmannstraße 15, 85748 Garching, Germany*
[b] *School of Mechanical and Aerospace Engineering, Queen's University Belfast, United Kingdom*
[c] *INEGI, Institute of Science and Innovation in Mechanical and Industrial Engineering, Rua Dr. Roberto Frias 400, 4200-465 Porto, Portugal*
[d] *CITAB, University of Tras-os-Montes e Alto Douro, UTAD, Quinta de Prados, 5000-801 Vila Real, Portugal*
[e] *DEMec, Faculdade de Engenharia, Universidade do Porto, Rua Dr. Roberto Frias, 4200-65 Porto, Portugal*

Abstract

This work presents an experimental method to measure the compressive crack resistance curve of fiber-reinforced polymer composites when subjected to dynamic loading. The data reduction couples the concepts of energy release rate, size effect law and R-curve. Double-edge notched specimens of four different sizes are used. Both split-Hopkinson pressure bar and quasi-static reference tests are performed. The full crack resistance curves at both investigated strain rate regimes are obtained on the basis of quasi-static fracture analysis theory. The results show that the steady state fracture toughness of the fiber compressive failure mode of the unidirectional carbon-epoxy composite material IM7-8552 is 165.6 kJ/m^2 and 101.6 kJ/m^2 under dynamic and quasi-static loading, respectively. Therefore the intralaminar fracture toughness in compression is found to increase with increasing strain rate.

Keywords: Fiber-reinforced composites, R-curve, Dynamic fracture, Size effect

*Corresponding author. Tel.: +49 8928915096; Fax: +49 8928915097. E-mail address: kuhn@lcc.mw.tum.de (P. Kuhn)

1. Introduction

Recently proposed strength analysis methods [1, 2, 3, 4, 5] require the specification of fracture toughness parameters associated to the main failure modes in order to predict damage evolution after the material strength has been reached. The softening laws used in the material models with progressive damage are dictated by the crack resistance curves (R-curves) [6] and therefore reliable experimental methods to measure the fracture toughnesses and corresponding crack resistance curves are needed.

While well established static test standards and procedures are available for the interlaminar matrix failure modes [7, 8, 9], no test standards exist to measure the intralaminar fracture toughness associated with the longitudinal failure of fiber-reinforced composites. Pinho et al. [10] suggested Compact Tension (CT) and Compact Compression (CC) tests to obtain fracture toughness values for fiber tensile and fiber compressive failure, respectively. However, the CC test specimen is inadequate to measure the R-curve, since i) the kink band onset and propagation is accompanied by secondary damage mechanisms (e.g. delamination) that are neglected and will results in a exaggerated estimation of the fracture toughness; ii) the crack tip cannot be easily identified; iii) the tractions within the fracture process zone are not taken into account properly [11]. Hence only the initiation value for the fiber compressive fracture toughness can be measured confidently using the CC specimen. Similar work has been done by Zobeiry et al. [12], testing CC and over-heigth compact tension (OCT) specimens with a quasi-isotropic layup. Initiation values for compressive fracture toughness of polymer composites have also been obtained by Laffan et al. [13] using a four-point bending configuration. Soutis et al. [14] tested multi-directional centre-notched compression specimens with various layups and notch lengths to investigate the influence of the number of 0° plies on the laminate compressive fracture toughness. To overcome the limitations of the CC test method, Catalanotti et al. [15] proposed a static test method using double-edge notched (DEN) specimens and the relation between the size effect law and the

R-curve. In follow-up works, the method was extended to tensile [16] and shear loading [17] and recently used by Pinto et al. [18] to measure the intralaminar crack resistance curves at extreme temperatures.

Taking into account that automotive and aeronautical polymer composite structures are subjected to dynamic loading scenarios (e.g. crash, foreign object impact), strain rate effects should be captured by advanced composite material models to predict initiation and evolution of damage accurately. The strain rate sensitivity of the stiffness and strength components of polymer composites has been intensively investigated and reviewed over the last decades [19, 20]. In addition, the experimental investigation of the dynamic interlaminar fracture toughnesses has received significant attention, motivated by the need to understand the delamination damage within composite laminates after low-energy impact. Published work on dynamic interlaminar fracture toughness was summarized by Jacob et al. [21], concluding that there is no agreement, either, on the trend of frature toughness with regard to strain rate or on the best suitable experimental and analysis procedure.

In contrast to the interlaminar fracture modes, very little is known regarding the effect of dynamic loading on the energy intensive intralaminar fiber failure modes. McCarroll [22] used a servo-hydraulic machine to test carbon-epoxy CT specimens at cross-head velocities up to 12 m/s. With increasing loading speed, a possible small decrease of the intralaminar fiber tensile fracture toughness was found. However, the range of values was within the scatter of the results.

Therefore, there is the need to develop experimental methods to measure the intralaminar fracture toughness in a dynamic loading scenario. In the presented work, the methodology proposed by Catalanotti et al. [15] to measure the mode I intralaminar R-curve in compression is extended to the case of dynamic loading. This approach uses the relations between the size effect law, initially proposed by Bažant and Planas [23], the energy release rate (ERR) and the R-curve. The method does not require the optical measurement of crack length, whose determination is found to be a main source of errors in fracture mechanic tests [24], and is particularly critical for high loading rate experiments, where

high speed cameras with reduced resolution are used. The dynamic tests are conducted on a split-Hopkinson pressure bar (SHPB), which is a widely-used setup for dynamic fracture tests [25]. Following Catalanotti et al. [15], double-edge notched compression (DENC) specimens are used for the determination of the size effect law. This specimen type is well suited for SHPB testing, as it is found to be nonsensitive to complex wave deflections that might cause undesirable mixed mode stress state during the loading of the specimen.

2. Analysis scheme

The analysis scheme of this work is based on the relations between the energy release rate, the R-curve and the size effect law. According to Bažant and Planas [23], if the energy release rate is an increasing function of the crack length (the specimen has a positive geometry) the ERR-curves G_I for different specimen sizes w_k, corresponding to the peak loads P_{uk}, are tangent to the R-curve R (Fig. 1). This relation can be used to measure the intralaminar R-curves of fiber reinforced polymers, as shown by Catalanotti et al. [15, 16].

[Figure 1 about here]

The energy release rate G_I in a balanced cross-ply laminate (with x and y as the preferred axes of the material) under tensile or compressive loading normal to the fracture surface (mode I) reads, for a crack propagating along x [26]:

$$G_I = \frac{1}{E}\sqrt{\frac{1+\rho}{2}}K_I^2 \tag{1}$$

where E denotes the laminate Young's modulus ($E = E_x = E_y$), K_I is the stress intensity factor and ρ is the dimensionless elastic parameter defined as [26]:

$$\rho = \frac{2s_{12} + s_{66}}{2\sqrt{s_{11}s_{22}}} \tag{2}$$

where s_{lm} are the components of the compliance matrix computed in the $x-y$ coordinate system. The stress intensity factor, K_I in Eq. (1), depends on the

specimen geometry and can be written for a double edge notched specimen (Fig. 2) as [26, 27]:

$$K_I = \sigma\sqrt{w}\sqrt{\phi(\alpha,\rho)} \tag{3}$$

in which σ is the remote stress, w is the characteristic size of the specimen (see Fig. 2) and $\phi(\alpha,\rho)$ is the dimensionless correction function for geometry and orthotropy including the shape parameter $\alpha = a/w$. Replacing Eq. (3) in Eq. (1), G_I yields:

$$G_I(a+\Delta a) = \frac{1}{E}\sqrt{\frac{1+\rho}{2}}w\sigma^2\phi\left(\alpha_0 + \frac{\Delta a}{w}, \rho\right) \tag{4}$$

where $\alpha_0 = a_0/w$ is the initial shape parameter (see Fig. 2) and Δa is the crack increment.

[Figure 2 about here]

Since there are not analytical solutions available, $\phi(\alpha,\rho)$ can be calculated numerically by applying the Virtual Crack Closure Technique (VCCT) [28]. Following [15], a two-dimensional Finite Element Model of the DENC specimen is built in the commercial software Abaqus [29] using 4-node reduced integration elements (CPS4R) with assigned elastic properties of the laminate (Fig. 3). The energy release rate, calculated with the VCCT, is equal to:

$$G_I(a^\star,\rho) = Y_m(a^\star,\rho)\, u_n(a^\star,\rho)/l_e \tag{5}$$

where $a^\star$ is the crack length of the given FE model, Y_m and u_n are the load and the displacement in the y-direction of the nodes m and n, respectively, and l_e is the element length in x-direction (see Fig. 3). Replacing $G_I(a^\star,\rho)$ in Eq. (4) yields $\phi(\alpha^\star,\rho)$. Repeating this calculation for several $\alpha^\star$ using a parametric model, and fitting the numerical point using a polynomial fitting function allows the calculation of $\phi(\alpha,\rho)$.

[Figure 3 about here]

The approach proposed by Bažant and Planas [23], that the crack driving force curve G_I at the peak load P_u is tangent to the R-curve R, is described by

the following system of equations:

$$\begin{cases} G_I(\Delta a) = R(\Delta a) \\ \frac{\partial G_I(\Delta a)}{\partial \Delta a} = \frac{\partial R(\Delta a)}{\partial \Delta a}. \end{cases} \tag{6}$$

Using the ultimate nominal stress, $\sigma_u = P_u/(2wt)$, where t is the laminate thickness, and assuming that the size effect law , $\sigma_u = \sigma_u(w)$, is known, substituting Eq. (4) in the first of Eq. (6) results in:

$$\frac{1}{E}\sqrt{\frac{1+\rho}{2}} w\sigma_u^2 \phi\left(\alpha_0 + \frac{\Delta a}{w}, \rho\right) = R(\Delta a) \tag{7}$$

which holds for every specimen size w. Remembering that, by definition, the R-curve does not depend on the spezimen size w ($\partial R/\partial w = 0$) and assuming that geometrically similar specimens are tested (α_0 is not a function of w) [23], the second of Eq. (6) yields:

$$\frac{1}{E}\sqrt{\frac{1+\rho}{2}} \frac{\partial}{\partial w}\left(w\sigma_u^2 \phi\left(\alpha_0 + \frac{\Delta a}{w}, \rho\right)\right) = 0. \tag{8}$$

Eq. (8) can be solved for $w = w(\Delta a)$ and replacing this solution in Eq. (7) yields the R-curve, $R(\Delta a)$. Visually, the R-curve is the envelope of the crack driving force curves at the peak load (see Fig. 1).

The described method provides the R-curve of the laminate. In fiber reinforced polymers the fracture toughness of the fiber failure modes is much higher than for matrix failure modes that can therefore be neglected [30]. This consideration is also true for interlaminar damage. It should be emphasized that in the experimental results presented in the following no extensive delamination was observed; therefore, it can be assumed confidently that the energy dissipated in the crack propagation is mainly due to the damage of the fiber. Hence, for a balanced cross-ply laminate, the R-curve of the 0° plies, $R_0(\Delta a)$, can be estimated, from the energy balance, as twice of the laminates R-Curve, $R(\Delta a)$, without a significant loss of accuracy [10].

3. Material and experimental procedures

3.1. Material and test specimens

The carbon-epoxy prepreg material system HexPly IM7-8552, which is commonly used in primary aerospace structures, was selected for this work. In accordance with the specified heat cycle [31], a panel with a $[0/90]_{8s}$ layup and a nominal thickness of 4 mm was cured in a hot press.

From the manufactured panel, double-edge notched compression (DENC) specimens were machined using a 1 mm diameter milling tool. A constant ratio of the geometric properties (length, width, initial crack length a_0) was held for all different specimen sizes (Fig. 4). The dimensions of the specimens were adopted from [15]. The shape of the initial crack tip does not affect the correct determination of the R-curve [16, 32] and was constant (semicircular, 1 mm of diameter) for all specimens. To enable the use of digital image correlation (DIC), the specimens were prepared by applying a random black-on-white speckle pattern.

[Figure 4 about here]

Table 1 shows the elastic properties of the laminate under quasi-static (QS) and high strain rate (HR, $\dot{\epsilon}_s \approx 100$ s^{-1}) conditions. The Young's modulus E and the Poisson's ratio ν_{xy} of the balanced cross-ply were obtained by separate compression tests with unnotched specimens and no strain rate sensitivity was found for E. The in-plane shear modulus G_{xy} was calculated accordingly to the classical lamination theory using as reference the values found in [33].

[Table 1 about here]

3.2. Quasi-static experimental setup

The quasi-static (QS) reference tests were carried out on a standard electromechanical testing machine (Hegewald & Peschke Inspect Table 100), equipped with a 100 kN load cell. The tests were conducted under displacement control

and a cross-head displacement rate of 0.15 mm/min was imposed. A self alignment device as described in [33] was used and friction between the loading parts and the specimen end-surfaces was minimized by a thin layer of molybdenum disulphide (MoS_2) paste.

The GOM ARAMIS-4M optical system was used for DIC measurement of the three-dimensional in plane strain field. It consisted of two CCD cameras with a resolution of 1728 $\times$ 2352 pixel^2, adjusted to capture a measuring volume of 35 $\times$ 26 mm^2 (length $\times$ width). A frame rate of 1 frame per second (fps) was used together with a shutter speed of 50 ms. Fig. 5 shows the quasi-static photomechanical setup.

[Figure 5 about here]

3.3. Dynamic experimental setup

The high strain rate (HR) compression tests were performed on a split-Hopkinson pressure bar (SHPB) system, as illustrated in Figure 6. The lengths of the steel striker-, incident- and transmission bars were 0.6, 2.6 and 1.3 m, respectively. The strain gauges on the incident-bar were located at 1.3 m and on the transmission bar at 0.3 m away from the bar-specimen interfaces. The bars diameter d_b (Table 2) was adapted to the particular tested specimen width and friction between the specimen and the bar end-faces was reduced by applying a thin layer of MoS_2 paste. To ensure that the axial strain rate was the same for every specimen size, a Finite Element Model was used to set the SHPB configuration in terms of the striker velocity v_s and the diameter d_{PS} and thickness t_{PS} of the copper pulse shaper (Table 2). Expecting a linear stress-strain behaviour of the specimens up to failure, a triangular shaped incident-wave is best suited to obtain nearly constant strain rates [34, 35]. The accuracy of the used SHPB system was ascertained by bars-together tests, documented in [36].

For the determination of the two-dimensional strain field using DIC, the specimen deformation was monitored by a single Photron FASTCAM SA-Z high speed camera. For all specimens, a frame rate of 300,000 fps with a corresponding resolution of 256 $\times$ 128 pixel^2 was chosen.

[Figure 6 about here]

[Table 2 about here]

3.4. Data reduction methods

3.4.1. Stress, strain and strain rate

In the case of the quasi-static tests, the ultimate remote stress σ_u was calculated by dividing the peak load P_u, measured from the load cell of the testing machine, by the specimen cross-section A_s, with $A_s = 2wt$.

For the high rate tests the axial stress component of the specimen σ_s can be calculated with the classic split-Hopkinson pressure bar analysis (SHPBA) [37, 38] by using 1-wave- and 2-wave-analysis:

$$\sigma_{s1} = \frac{A_b}{A_s} E_b \varepsilon_T \tag{9}$$

$$\sigma_{s2} = \frac{A_b}{A_s} E_b (\varepsilon_I + \varepsilon_R) \tag{10}$$

where A_b is the bar cross-section, E_b is the Young's modulus of the bar material and ε_I, ε_R, ε_T are the incident, reflected and transmitted bar strain waves, respectively. As both terms (Eq. 9, Eq. 10) were used to check and confirm specimen stress-equilibrium, ultimate remote stress was calculated just from Eq. 9. The transmission wave ε_T in Eq. 9 has a smooth signal and dispersion effects in ε_T are small due to the short distance between the bar-specimen interface and the strain gauge terminal on the transmission bar (0.3 m). Since the specimen strain ε_s calculated from SHPBA tends to be over-predicted [39], specimen strain was obtained for all tests from the DIC Software GOM ARAMIS by calculating the nominal engineering strain between two facet points along the specimen center line, as illustrated in Figure 7. To ensure comparability, the same procedure was used to estimate the specimen strain in the quasi-static tests. The DIC analysis parameters were chosen accordingly to the resolutions of the camera images and are given in Table 3.

[Figure 7 about here]

[Table 3 about here]

The specimen strain was further used to obtain the specimen strain rate $\dot{\epsilon}_s$ in loading direction by applying finite differentiation:

$$\dot{\epsilon}_s(t) = \frac{\varepsilon_s(t) - \varepsilon_s(t - \Delta t)}{\Delta t} \tag{11}$$

in which Δt is the timestep between two consecutive DIC images.

3.4.2. Energy terms

The analysis scheme of this work (see section 2) is based on the quasi-static fracture mechanics theory. According to Jiang and Vecchio [25], quasi-static fracture theory is applicable for dynamic fracture toughness measurements under the condition of stress equilibrium. In addition to this classical split-Hopkinson bar equilibrium check (using Eq. 9 and Eq. 10), the energy terms of the specimens were calculated and analyzed by using DIC data. This analysis procedure therefore uses the true specimen deformation behaviour, obtained from the optical measurement. According to the law of conservation of energy for a continuum body, the balance of mechanical energy reads [40]:

$$\mathcal{W} = \mathcal{U} + \mathcal{K} \tag{12}$$

where $\mathcal{W}$ is the external work, which is stored in the structure as strain energy $\mathcal{U}$ and kinetic energy $\mathcal{K}$. When $\mathcal{K} \ll \mathcal{U}$ and fracture is the only energy-consuming process, quasi-static fracture mechanics theory is applicable [23]. Using the in-plane strain vector obtained from DIC, the strain energy of the specimen $\mathcal{U}$ is the sum of the strain energy at each individual facet point $\mathcal{U}_j$ and can be calculated as:

$$\mathcal{U} = \sum_j \mathcal{U}_j = \sum_j V_j \frac{1}{2}(E_x \varepsilon_{xj}^2 + E_y \varepsilon_{yj}^2 + G_{xy} \gamma_{xyj}^2) \tag{13}$$

in which ε_{xj}, ε_{yj} and γ_{xyj} are the individual facet's transversal, longitudinal and shearing strain, respectively. V_j is the associated volume of the individual facet point, regulated by the DIC analysis parameters (Table 3) and specimen's

thickness. The kinetic energy of the specimen $\mathcal{K}$ is calculated accordingly on basis of the velocity field from DIC:

$$\mathcal{K} = \sum_j \mathcal{K}_j = \sum_j \frac{1}{2} D V_j (v_{xj}^2 + v_{yj}^2) \tag{14}$$

where v_{xj} and v_{yj} are the individual facet's transversal and longitudinal velocity, respectively, and D is the density of the laminate.

4. Experimental results

4.1. Specimen deformation and failure

For each specimen type and strain rate regime, three valid tests are performed. All specimens fail due to compressive fracture along the direction of the initial notch, as shown in Fig. 8(a) for two specimens of type C. The axial (Fig. 8(b)) and shear strain fields (Fig. 8(c)) show plausible axis-symmetric and point-symmetric strain distributions, respectively, indicating well aligned loading of the specimens. Good accordance can be found between the strain distributions at quasi-static and dynamic loading conditions, which denote that no complex stress state is caused in the dynamically tested specimens due to wave deflections. Particularly, no shear strain is detected in the region near the crack tip at the specimen center, which verifies the assumption of crack propagation as a result of mode I loading.

[Figure 8 about here]

4.2. Stress-strain behaviour

Fig. 9 shows representative stress-strain curves for the different specimen sizes, tested at QS strain rate level (see Appendix A for all stress-strain curves). Nearly linear elastic behaviour is detected until the specimens failed by ultimate compressive failure at peak load.

[Figure 9 about here]

In Fig. 10, characteristic bar strain wave groups of a SHPB-test are presented[1]. The incident wave shows the desired triangular shape which causes a nearly constant strain rate in the specimen, indicated by the plateau in the reflected strain wave signal [38]. The point of the specimen's ultimate failure is expressed by a sharp rise of ε_R and, as the transmitted wave is proportional to the stress in the specimen (Eq. 9), by a sharp drop of ε_T, respectively. The bar strain waves are used to verify dynamic equilibrium of the specimen, by calculating and comparing the 1-wave (Eq. 9) and the 2-wave (Eq. 10) stress-time signals, plotted in Fig. 11. Despite the existence of small oscillations in the 2-wave stress-time signal, it can be stated that the DENC-specimen is in dynamic stress equilibrium before the occurrence of ultimate failure. Following the classic SHPB theory [38], this implies that the specimen stress can be calculated correctly from the bar strain waves. Furthermore, the existence of the stress equilibrium enables the use of the quasi-static fracture theory to obtain the fracture toughness properties [25].

[Figure 10 about here]

[Figure 11 about here]

Representative stress-strain curves, obtained at the SHPB, are reported in Fig. 12 for the different specimen sizes (see Appendix A for all stress-strain curves). The comparison with the stress-strain curves from QS tests (Fig. 9) shows that the axial stiffness under dynamic loading is equal, but the HR specimens fail at a higher stress and strain level than the QS specimens. The corresponding strain rate curves for both investigated loading regimes are shown in Fig. 13. The strain rate of the QS tests is in the order between 2×10^{-5} s^{-1} and 1×10^{-4} s^{-1}, which is a typical magnitude for quasi-static loading conditions [41]. For the HR tests a nearly constant strain rate of about 100 s^{-1} was achieved for all specimen types, allowing a reliable comparison with each other.

[1]The chosen specimen type C was used for a number of other figures presented in this paper: Fig. 10 can be linked to Figs. 11, 12 and 13.

[Figure 12 about here]

[Figure 13 about here]

Fig. 14 shows the plot of the ultimate stress σ_u vs. the specimen size w. As a results of the size effect, the ultimate stress decreases with increasing specimen size at both investigated strain rate regimes [23]. Furthermore, a pronounced strain rate effect can be measured. Compared to the QS results, the ultimate stress at $\dot{\epsilon}_s \approx 100$ s^{-1} for specimen type A, B, C and D increases by 23%, 35%, 29% and 28%, respectively. Table 4 summarizes the results for the two investigated strain rate regimes.

[Figure 14 about here]

[Table 4 about here]

4.3. Energy terms

The terms of strain and kinetic energy, calculated with Eqs. (13) and (14), are shown exemplarily in Fig. 15 for specimen size D (see Appendix B for energy terms of other specimen sizes). At both strain rate regimes, strain energy increases approximately quadratically over time until ultimate failure occur (at the last plotted data point). The main part of the overall strain energy $\mathcal{U}$ is contributed from the energy portion in loading direction $\mathcal{U}_y$ (see Fig. 2). The strain energy at failure of the HR specimen is higher than for the QS specimen, which is plausible due to the higher strain at failure at nearly unchanged stiffness (see Table 3 and Figs. 9 and 12). Under quasi-static loading, the kinetic energy $\mathcal{K}$ is quite constant at a very low level after initial acceleration (Fig. 15(c)). At failure, the ratio of $\mathcal{U}/\mathcal{K}$ is in the order of 10^{12} and therefore $\mathcal{K} \ll \mathcal{U}$, as characteristic for quasi-static loading. The kinetic energy during dynamic testing is found to increase over time (Fig. 15(d)). In contrast to an electromechanical testing machine, where one specimen interface is at rest while the other is loaded by the cross-head displacement, both bar-specimen interfaces are in motion at an SHPB test. The specimen is therefore deformed by the relative displacement

between the two interfaces and the kinetic energy in the specimen during SHPB testing comes partially from the superposed rigid body movement of the DENC-specimen. For the HR tests, the ratio of $\mathcal{U}/\mathcal{K}$ at ultimate failure was calculated to be 315, 163, 158 and 91 for specimen type A, B, C and D, respectively, and is therefore significant higher than during the QS tests. However, even in the worst case (specimen type D), the kinetic energy $\mathcal{K}$ is just about 1% of the strain energy $\mathcal{U}$ at failure. Therefore quasi-static fracture mechanics seem to be applicable for the analysis of the SHPB-tests without any significant error. It should be noted that this conclusions is based on the analysis of the overall specimen deformation behaviour, not taking into account very local effects that may occur near the crack tip.

[Figure 15 about here]

5. Obtaining the Fracture Toughness Properties

According to the analysis scheme (presented in Section 2 of the article), the size effect law $\sigma_u = \sigma_u(w)$ must be known to obtain the fracture toughness properties of the material. To find the relation between the ultimate nominal stress and the size of the specimen, Bažant and Planas [23] suggested different kinds of linear and bilogarithmic regression plots, all leading to very similar results for the R-curve. For the experimental results of the IM7-8552 DENC specimens (Section 4), a best fit was obtained for both QS and HR results by using the following linear regression [23]:

$$\sigma_u^{-2} = mw + q \tag{15}$$

in which m and q are the slope and the intercept of the linear curve fit, respectively. In Fig. 16, σ_u^{-2} vs. w and the corresponding linear fitting curves are plotted for both investigated strain rate regimes. The curve fitting parameters and the respective coefficient of determination R^2 are listed in Table 5.

[Figure 16 about here]

[Table 5 about here]

All parameters of the analysis scheme apart from the size effect law can be calculated on basis of the material and specimen geometry data (Section 3). Fig. 17 shows the plot of the dimensionless correction function ϕ over the shape parameter $\alpha = a/w$ for the QS and HR material data sets.

[Figure 17 about here]

With the defined size effect law, the R-curve of the laminate R can be calculated by solving Eq. (8) for $w = w(\Delta a)$ and substituting this solution in Eq. (7). Finally, the R-curve of the 0° plies R_0 is twice the value of R for every Δa. The R_0-curves for both investigated strain rate regimes are presented in Fig. 18, showing that the compressive intralaminar fracture toughness of the 0° plies under HR loading is considerably larger than that obtained under QS loading.

[Figure 18 about here]

For the chosen linear regression of the size effect law, the steady-state value of the fracture toughness R^0_{ss} can be calculated as [23]:

$$R^0_{ss} = \lim_{w\to\infty} R_0 = \frac{\sqrt{2(1+\rho)}}{E}\frac{\phi_0}{m} \tag{16}$$

where $\phi_0 = \phi|_{\alpha=\alpha_0}$. The length of the fracture process zone l_{fpz} in case of linear regression is [23]:

$$l_{fpz} = \frac{f_0}{2f'_0}\frac{q}{m} \tag{17}$$

where $f_0 = \sqrt{\phi}|_{\alpha=\alpha_0}$ and $f'_0 = \partial\sqrt{\phi}/\partial\alpha|_{\alpha=\alpha_0}$. The values obtained for R^0_{ss} and l_{fpz} are summarized in Table 6. Table 6 also includes the corresponding coefficients of variation (CV), that are calculated according to Bažant and Planas [23] under additional consideration of the Young's modulus deviation.

[Table 6 about here]

The steady-state value of the fracture toughness R^0_{ss} under HR loading ($R^{HR}_{ss} = 165.6$ kJ/m^2) is found to be 63% higher than the QS value ($R^{QS}_{ss} = 101.6$ kJ/m^2). Despite the fact that the same composite material was used, the measured R^{QS}_{ss} value measured in the present workis higher than the value calculated with the same procedure by Catalanotti et al. [15] ($R^0_{ss} = 61$ kJ/m^2). However, a lower value for the laminate Young's modulus for IM7-8552 was used in the presented work, which has a significant influence on R^{QS}_{ss} according to Eq. (16). It should further be noted, that initiation values of 47.5 kJ/m^2 and 25.9 kJ/m^2, measured with compact compression [11] and four-point bending specimens [13], respectively, represent just single points on the rising part of the R_0-curve.

As for R^0_{ss}, the calculated values for the length of the fracture process zone l_fpz also indicate a strain rate effect, however the values are within the scatter of the results.

To simplify the use of the measured R-curves, Bažant and Planas [23] recommend to express them in an analytical form by using the following equation:

$$\begin{cases} R_0 = R_{ss}\left[1-(1-\kappa\Delta a)^n\right] & if \Delta a < l_{fpz} \\ R_0 = R_{ss} & if \Delta a \geq l_{fpz} \end{cases} \tag{18}$$

in which κ and n are the parameters to fit the points obtained by solving Eqs. (7) and (8). The optimal parameters for both investigated strain rate regimes are listed in Table 7.

[Table 7 about here]

6. Conclusions

The presented work shows that the R-curve for the fiber compressive failure mode can be reliably measured for dynamic loading conditions, using the relations between the size effect law, the energy release rate and the R-curve.

It can be concluded, that the used double-edged notched specimens are well suitable for dynamic tests on a split-Hopkinson pressure bar setup. No significant difference could be found between the strain distributions, obtained from

DIC, at quasi-static and high rate tests and the assumption of mode I could be verified for both investigated strain rate regimes. Furthermore, the DIC data enabled the calculation and comparison of the strain energy and kinetic energy terms, indicating that quasi-static fracture theory can be used without any significant error. In addition, stress equilibrium and a nearly constant strain rate of about 100 s^{-1} was achieved for all tested specimen sizes at the SHPB, ensuring a reliable determination of the size effect law.

For the investigated carbon-epoxy material IM7-8552, the R-curve for fiber compressive failure under high rate loading is increased compared to the quasi-static R-curve. The steady-state value of the fracture toughness under dynamic loading is 165.6 kJ/m^2 and therefore 63% higher than the quasi-static value of 101.6 kJ/m^2. The length of the fracture process zone also increases from 2.05 mm to 2.24 mm with increasing strain rate.

The results of the presented work contribute to a further understanding of the complex material response of polymer composite materials. It can be used to further enhance state-of-the art composite material models and therefore contributes to a more effective use of composite materials in primary automotive and aeronautical structures, where dynamic load scenarios must be considered during the design phase. With the presented results and earlier research published by the authors [33, 34, 42], a comprehensive dynamic material data set for the carbon-epoxy material IM7-8552 now exists.

Acknowledgements

The authors would like to acknowledge Dr. Iman Taha and Christina Aust from Fraunhofer Institution for Casting, Composite and Processing Technology (IGCV) for providing the Photron FASTCAM SA-Z high speed camera. The presented research did not receive a specific grant from funding agencies in the public, commercial, or not-for-profit sectors.

Appendix A. Stress-strain curves

The stress-strain curves of the specimen sizes A, B, C and D are shown in Fig. A.1, Fig. A.2, Fig. A.3 and Fig. A.4, respectively.

[Figure A.1 about here]

[Figure A.2 about here]

[Figure A.3 about here]

[Figure A.4 about here]

Appendix B. Energy terms

Fig. B.1, Fig. B.2 and Fig. B.3, show energy terms of specimen sizes A, B and C, respectively (for specimen size D see Fig. 15).

[Figure B.1 about here]

[Figure B.2 about here]

[Figure B.3 about here]

References

[1] Lapczyk I, Hurtado JA. Progressive damage modeling in fiber-reinforced materials. Composites: Part A 2007;38:2333–2341. doi:10.1016/j.compositesa.2007.01.017.

[2] Maimí P, Camanho PP, Mayugo JA, Dávila CG. A continuum damage model for composite laminates: Part II - Computational implementation and validation. Mechanics of Materials 2007;39:909–919. doi:10.1016/j.mechmat.2007.03.006.

[3] Camanho PP, Bessa MA, Catalanotti G, Vogler M, Rolfes R. Modeling the inelastic deformation and fracture of polymer composites Part II: Smeared crack model. Mechanics of Materials 2013;59:36–49. doi:10.1016/j.mechmat.2012.12.001.

[4] Williams KV, Vaziri R, Poursartip A. A physically based continuum damage mechanics model for thin laminated composite structures. International Journal of Solids and Structures 2003;40:2267–2300. doi:110.1016/S0020-7683(03)00016-7.

[5] Forghani A, Zobeiry N, Poursartip A, Vaziri R. A structural modelling framework for prediction of damage development and failure of composite laminates. Journal of Composite Materials 2013;47:2553–2573. doi:10.1177/0021998312474044.

[6] Dávila CG, Rose CA, Camanho PP. A procedure for superimposing linear cohesive laws to represent multiple damage mechanisms in the fracture of composites. International Journal of Fracture 2009;158:211–223. doi:10.1007/s10704-009-9366-z.

[7] ASTM D5528-13, Standard test method for mode I interlaminar fracture toughness of unidirectional fiber-reinforced polymer matrix composites, ASTM International, West Conshohocken, PA. 2013. doi:10.1520/D5528.

[8] DIN EN 6033, Aerospace series - Carbon fibre reinforced plastics - Test method - Determination of interlaminar fracture toughness energy - Mode I - GIC; German and English version EN 6033:2015. 2015.

[9] DIN EN 6034, Aerospace series - Carbon fibre reinforced plastics - Test method - Determination of interlaminar fracture toughness energy - Mode II - G[IIC]; German and English version EN 6034:2015. 2015.

[10] Pinho ST, Robinson P, Iannucci L. Fracture toughness of the tensile and compressive fibre failure modes in laminated composites. Composites Sci-

ence and Technology 2006;66:2069–2079. doi:10.1016/j.compscitech.2005.12.023.

[11] Catalanotti G, Camanho PP, Xavier J, Dávila CG, Marques AT. Measurement of resistance curves in the longitudinal failure of composites using digital image correlation. Composites Science and Technology 2010;70:1986–1993. doi:10.1016/j.compscitech.2010.07.022.

[12] Zobeiry N, Vaziri R, Poursartip A. Characterization of strain-softening behavior and failure mechanisms of composites under tension and compression. Composites: Part A 2015;68:29–41. doi:110.1016/S0020-7683(03)00016-7.

[13] Laffan MJ, Pinho ST, Robinson P, Iannucci L, McMillan A. Measurement of the fracture toughness associated with mode I fibre compressive failure. In: 14th European Conference on Composite Materials, Budapest, Hungary; 2010.

[14] Soutis C, Curtis PT, Fleck NA. Compressive failure of notched carbon fibre composites. Proceedings: Mathematical and Physical Sciences 1993;440:241–256.

[15] Catalanotti G, Xavier J, Camanho PP. Measurement of the compressive crack resistance curve of composites using the size effect law. Composites: Part A 2014;56:300–307. doi:10.1016/j.compositesa.2013.10.017.

[16] Catalanotti G, Arteiro A, Hayati M, Camanho PP. Determination of the mode I crack resistance curve of polymer composites using the size-effect law. Engineering Fracture Mechanics 2014;118:49–65. doi:10.1016/j.engfracmech.2013.10.021.

[17] Catalanotti G, Xavier J. Measurement of the mode II intralaminar fracture toughness and R-curve of polymer composites using a modified Iosipescu specimen and the size effect law. Engineering Fracture Mechanics 2015;138:202–214. doi:10.1016/j.engfracmech.2015.03.005.

[18] Pinto RF, Catalanotti G, Camanho PP. Measuring the intralaminar crack resistance curve of fibre reinforced composites at extreme temperatures. Composites: Part A 2016;91:145–155. doi:10.1016/j.compositesa.2016.10.004.

[19] Sierakowski RL. Strain rate effects in composites. Applied Mechanics Reviews 1997;50:741–761. doi:10.1115/1.3101860.

[20] Jacob GC, Starbuck JM, Fellers JF, Simunovic S, Boeman RG. Strain rate effects on the mechanical properties of polymer composite materials. Journal of Applied Polymer Science 2004;94:296–301. doi:10.1002/app.20901.

[21] Jacob GC, Starbuck JM, Fellers JF, Simunovic S, Boeman RG. The effect of loading rate on the fracture toughness of fiber reinforced polymer composites. Journal of Applied Polymer Science 2005;96:899–904. doi:10.1002/app.21535.

[22] McCarroll C. High rate fracture toughness measurements of laminated composites. Ph.D. thesis; Imperial College London; 2011.

[23] Bažant ZP, Planas J. Fracture and size effect in concrete and other quasibrittle materials. CRC Press LLC, Boca Raton, Florida, USA; 1998.

[24] Laffan MJ, Pinho ST, Robinson P, McMillan A. Translaminar fracture toughness testing of composites: a review. Polymer Testing 2012;31:481–489. doi:10.1016/j.polymertesting.2012.01.002.

[25] Jiang F, Vecchio KS. Hopkinson bar loaded fracture experimental technique: A critical review of dynamic fracture toughness tests. Applied Mechanics Reviews 2009;62:1–39. doi:10.1115/1.3124647.

[26] Suo Z, Bao G, Fan B, Wang TC. Orthotropy rescaling and implications for fracture in composites. International Journal of Solids and Structures 1990;28:235–248.

[27] Bao G, Ho S, Suo Z, Fan B. The role of material orthotropy in fracture specimens for composites. International Journal of Solids and Structures 1992;29:1105–1116.

[28] Krueger R. The virtual crack closure technique: History, approach and applications. Technical Report NASA/CR-2002-211628. Tech. Rep. ICASE Report No. 2002-10; ICASE, Hampton, Virginia, USA; 2002.

[29] Dassault Systèms. Abaqus Version 6.14-2 Documentation. 2014.

[30] Laffan MJ, Pinho ST, Robinson P, Iannucci L. Measurement of the in situ ply fracture toughness associated with mode I fibre tensile failure in FRP. Part II: Size and lay-up effects. Composites Science and Technology 2010;70:614–621. doi:10.1016/j.compscitech.2009.12.011.

[31] Hexcel Product Data Sheet: HexPly 8552 Epoxy matrix. 2016. URL: http://www.hexcel.com/user_area/content_media/raw/HexPly_8552_eu_DataSheet.pdf.

[32] Jackson WC, Ratcliffe JG. Measurement of fracture energy for kink-band growth in sandwich specimens. In: Proceedings of the 2nd international conference on composites testing and model identification, Comptest 2004, University of Bristol, Bristol, UK; 2004.

[33] Koerber H, Xavier J, Camanho PP. High strain rate characterisation of unidirectional carbon-epoxy IM7-8552 in transverse compression and in-plane shear using digital image correlation. Mechanics of Materials 2010;42:1004–1019. doi:10.1016/j.mechmat.2010.09.003.

[34] Koerber H, Camanho PP. High strain rate characterisation of unidirectional carbon-epoxy IM7-8552 in longitudinal compression. Composites Part A 2011;42:462–470. doi:10.1016/j.compositesa.2011.01.002.

[35] Nemat-Nasser S, Isaacs JB, Starrett JE. Hopkinson techniques for dynamic recovery experiments. Proceedings: Mathematical and Physical Sciences 1991;435:371–391.

[36] Koerber H, Xavier J, Camanho PP, Essa YE, de la Escalera FM. High strain rate behaviour of 5-harness-satin weave fabric carbonepoxy composite under compression and combined compressionshear loading. International Journal of Solids and Structures 2015;54:172–182. doi:10.1016/j.ijsolstr.2014.10.018.

[37] Kolsky H. An investigation of the mechanical properties of materials at very high rates of loading. Proc Phys Soc London 1949;Sect. B. 62 (II-B):676–700.

[38] G. T. Gray III . Classic split-Hopkinson pressure bar testing. In: ASM handbook mechanical testing and evaluation; vol. 8. ASM International Ohio USA; 2000, pp. 462-476.

[39] Gama BA, Gillespie JW. Numerical hopkinson bar analysis: uni-axial stress and planar bar-specimen interface conditions by design. Tech. Rep. ARL-CR-553; Army Research Laboratory, USA; 2004.

[40] Mase GT, Smelser RE, Mase GE. Continuum mechanics for engineers. CRC Press LLC, Boca Raton, Florida, USA; 2010.

[41] S. Nemat-Nasser . Introduction to high strain rate testing. In: ASM handbook mechanical testing and evaluation; vol. 8. ASM International Ohio USA; 2000.

[42] Kuhn P, Ploeckl M, Koerber H. Experimental investigation of the failure envelope of unidirectional carbon-epoxy composite under high strain rate transverse and off-axis tensile loading. In: 11th International Conference on the Mechanical and Physical Behaviour of Materials under Dynamic Loading, Lugano, Switzerland, 2015; vol. 94. 2015, p. 01040 1–6. doi:10.1051/epjconf/20159401040.

Figures

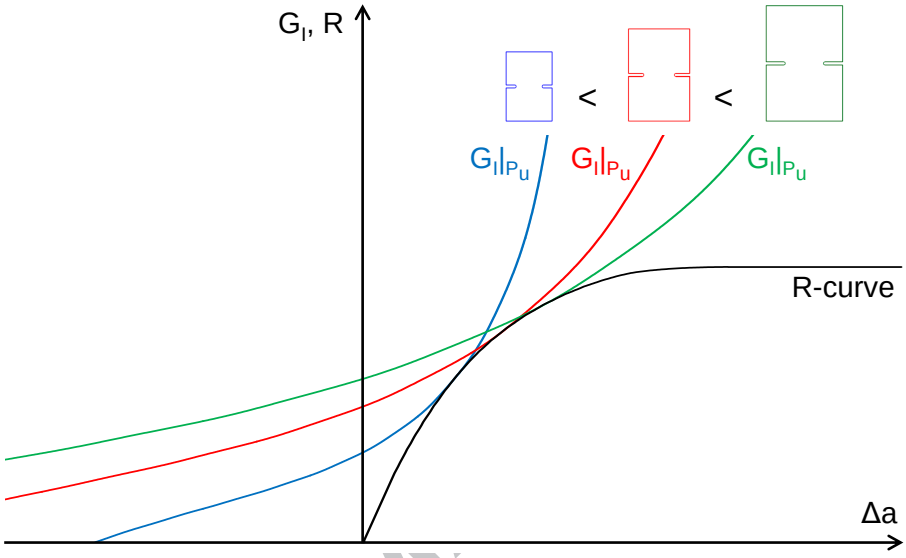

Figure 1: Crack driving force curves G_I for different specimen sizes at respective peak load P_u and R-curve.

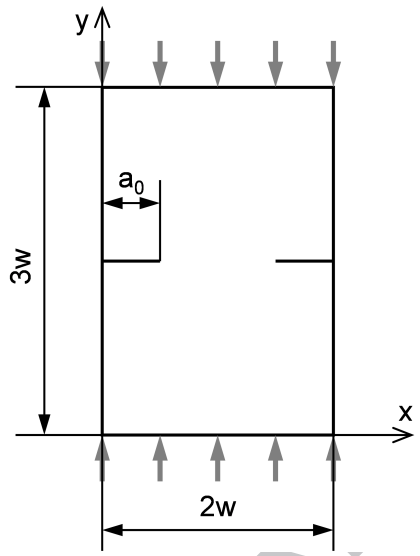

Figure 2: Double edge notched compression (DENC) specimen.

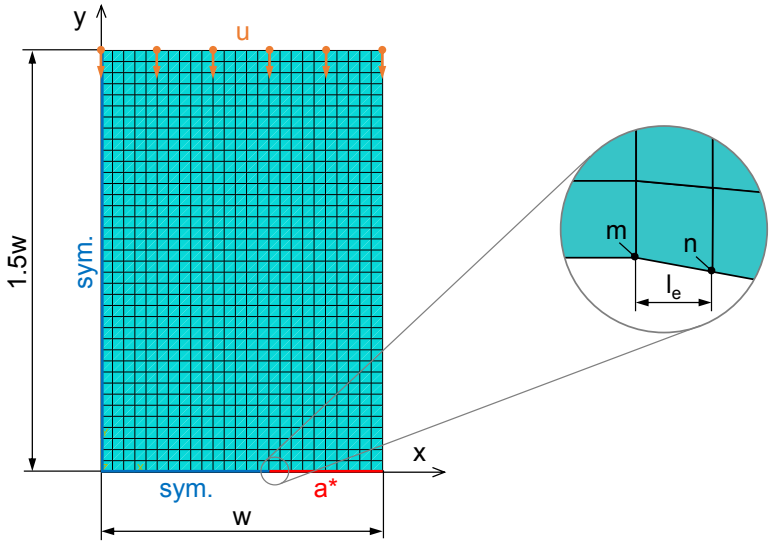

Figure 3: Finite element model used for application of VCCT.

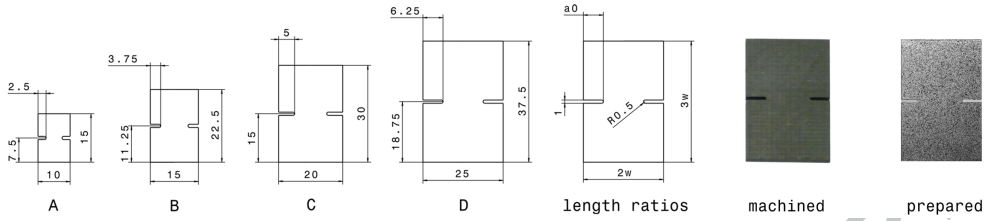

Figure 4: Used specimen sizes (dimensions in mm), machined and prepared specimen for DIC measurement (size D).

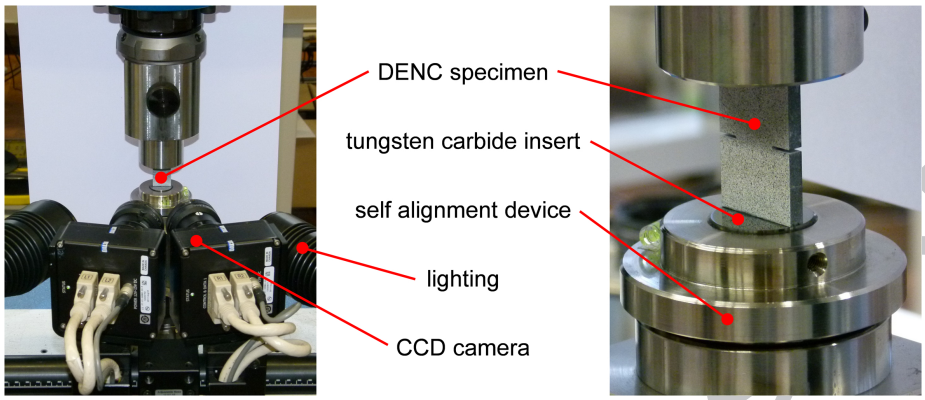

Figure 5: Compression setup for quasi-static tests.

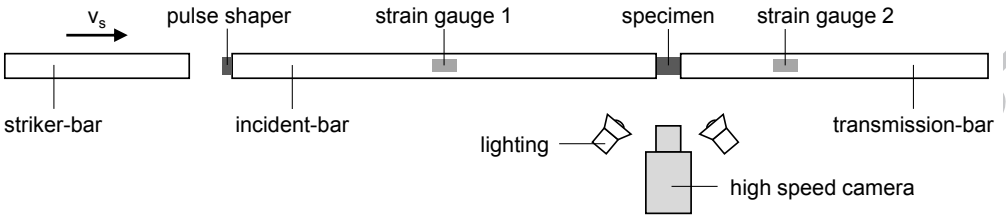

Figure 6: Split-Hopkinson pressure bar (SHPB) setup for dynamic tests.

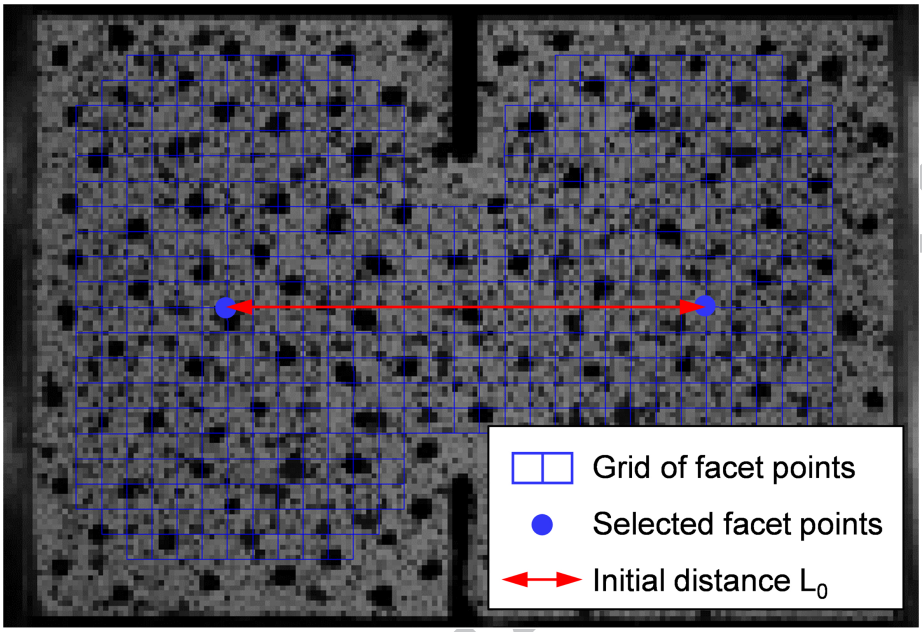

Figure 7: Aramis analysis parameters on DENC-specimen (specimen size D).

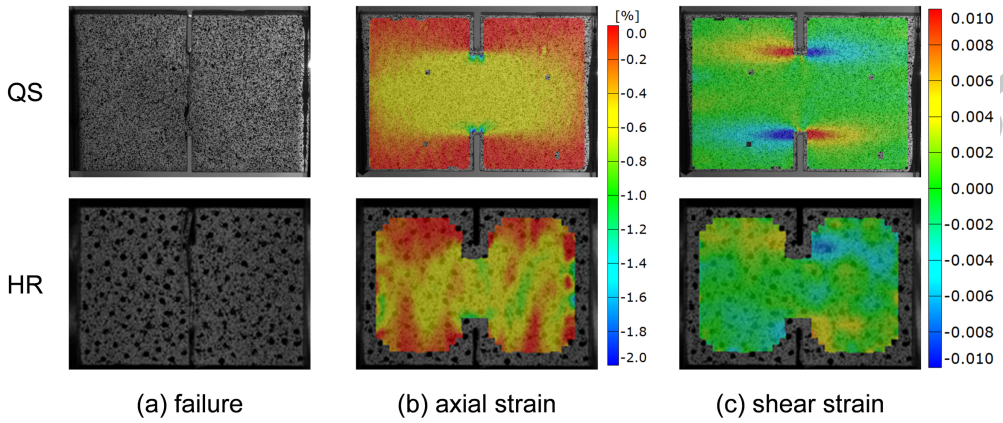

Figure 8: Failed specimens (a) and strain fields at same axial strain level ($\epsilon \approx 0.5\%$) (b, c) under QS and HR loading (specimen size C, QS images are rotated 90 counterclockwise).

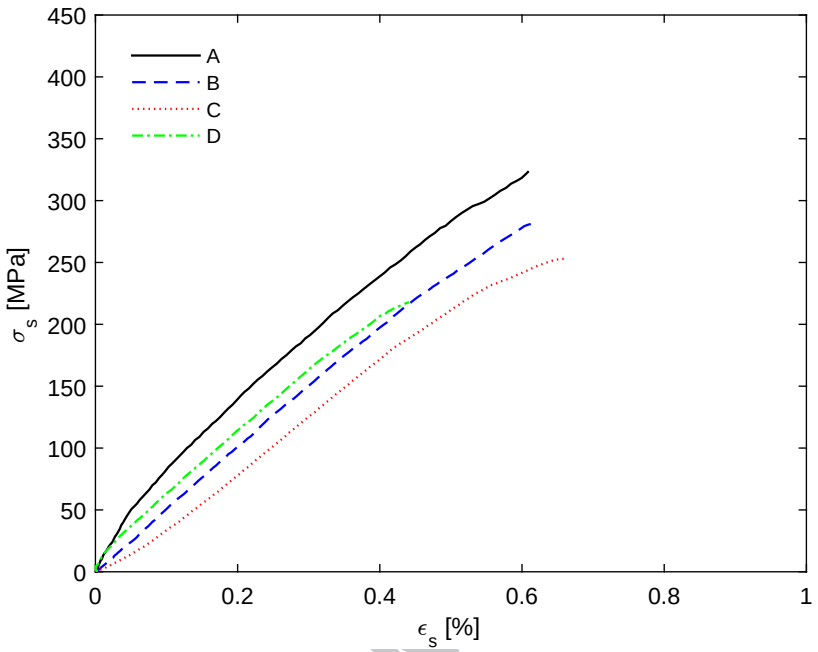

Figure 9: Stress-strain response for QS loading.

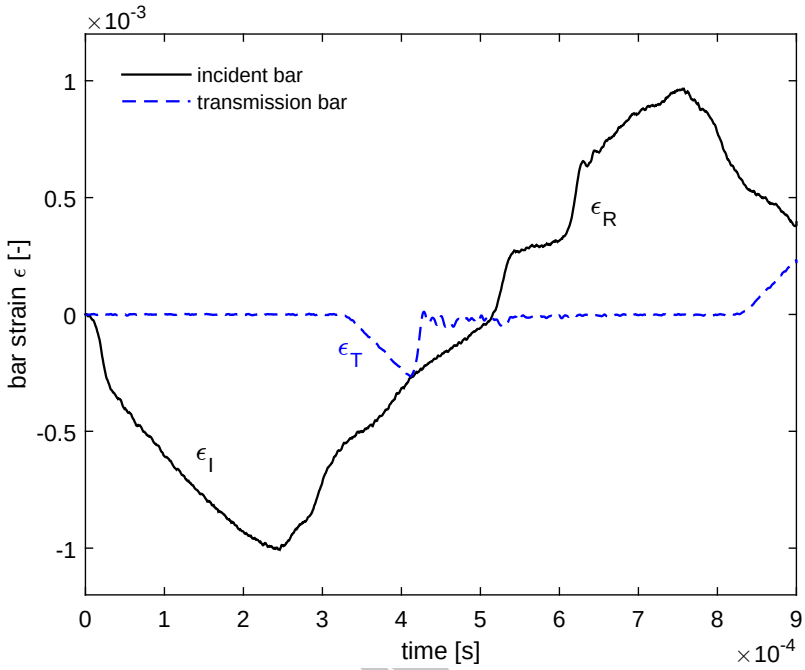

Figure 10: Example of a bar strain wave group of an SHPB test (specimen size C).

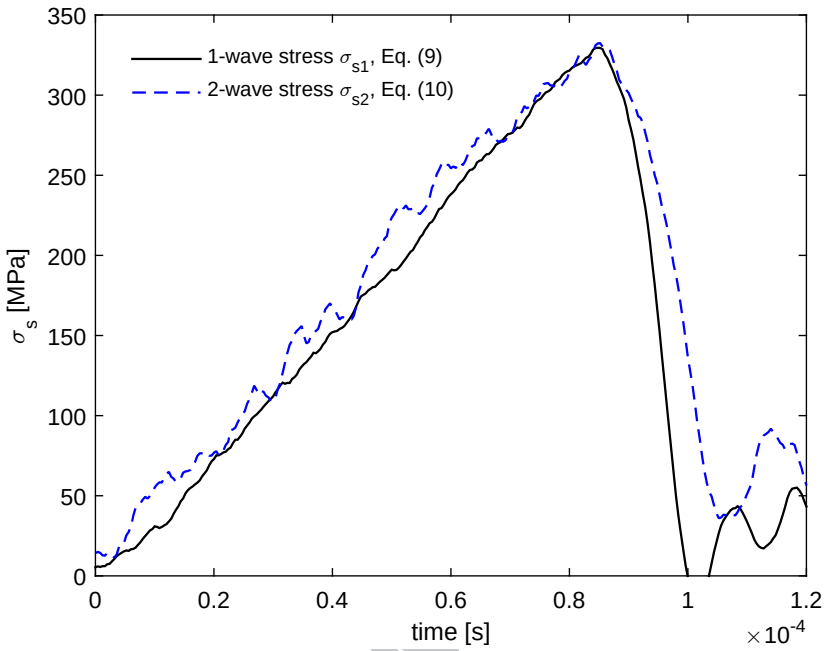

Figure 11: Example of a dynamic stress equilibrium check (specimen size C).

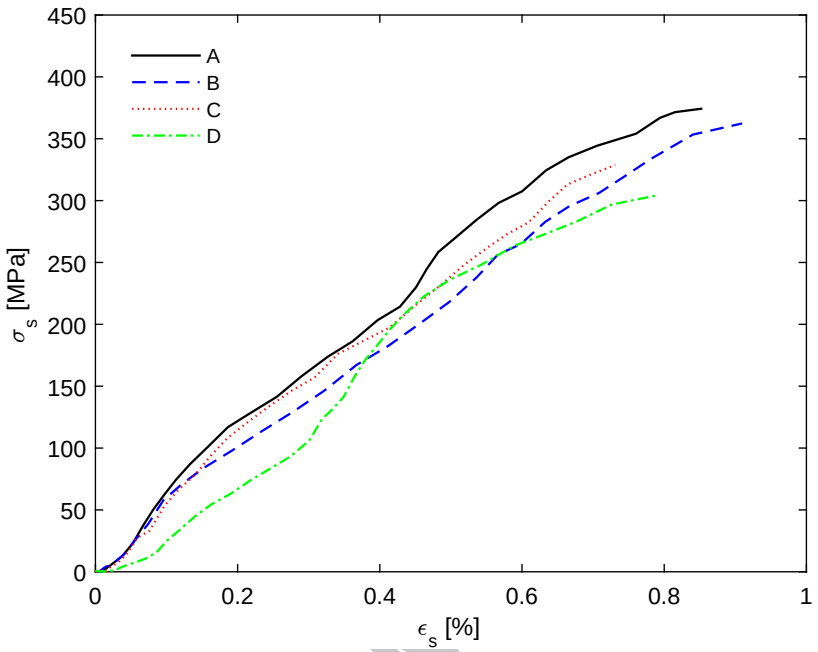

Figure 12: Stress-strain response for HR loading.

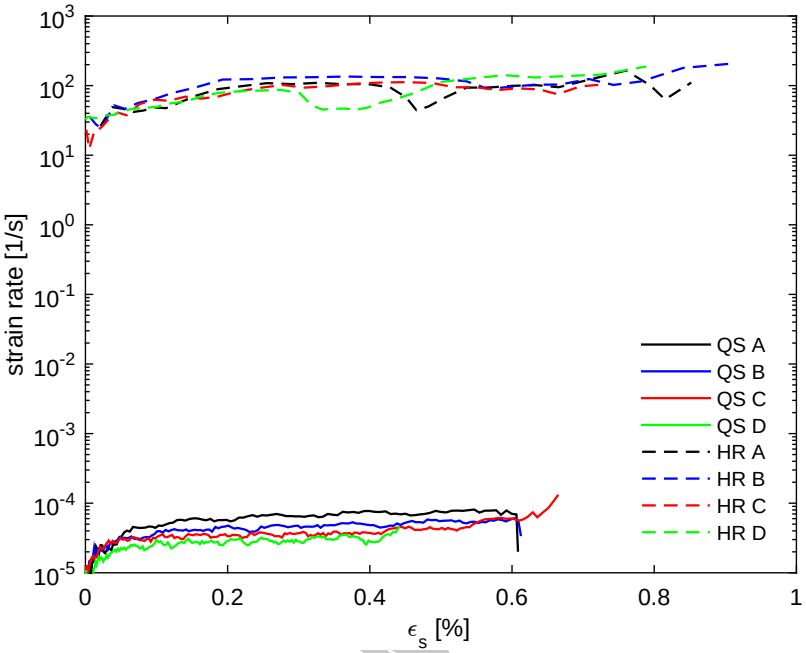

Figure 13: Specimen strain rate curves for QS and HR loading.

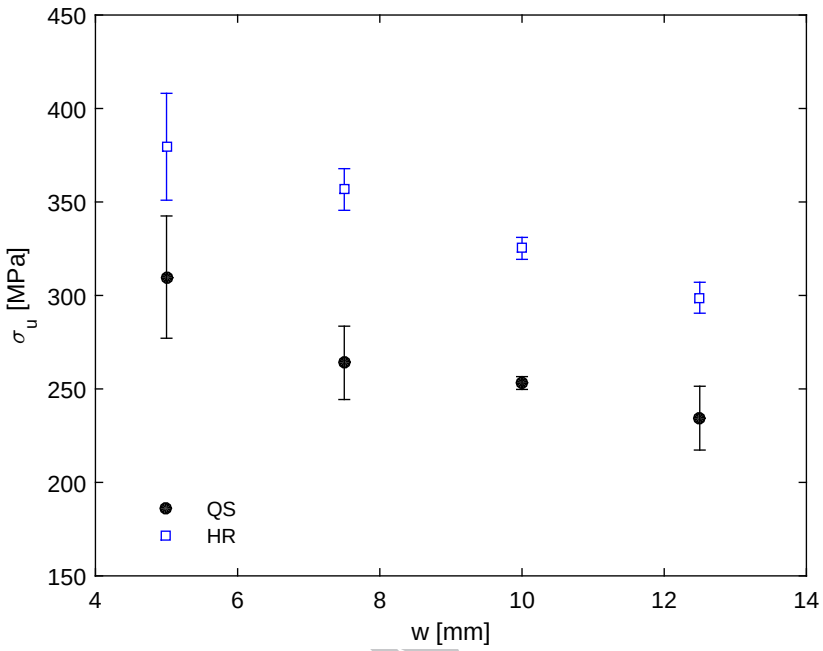

Figure 14: Ultimate stress σ_u vs. specimen size w for QS and HR loading.

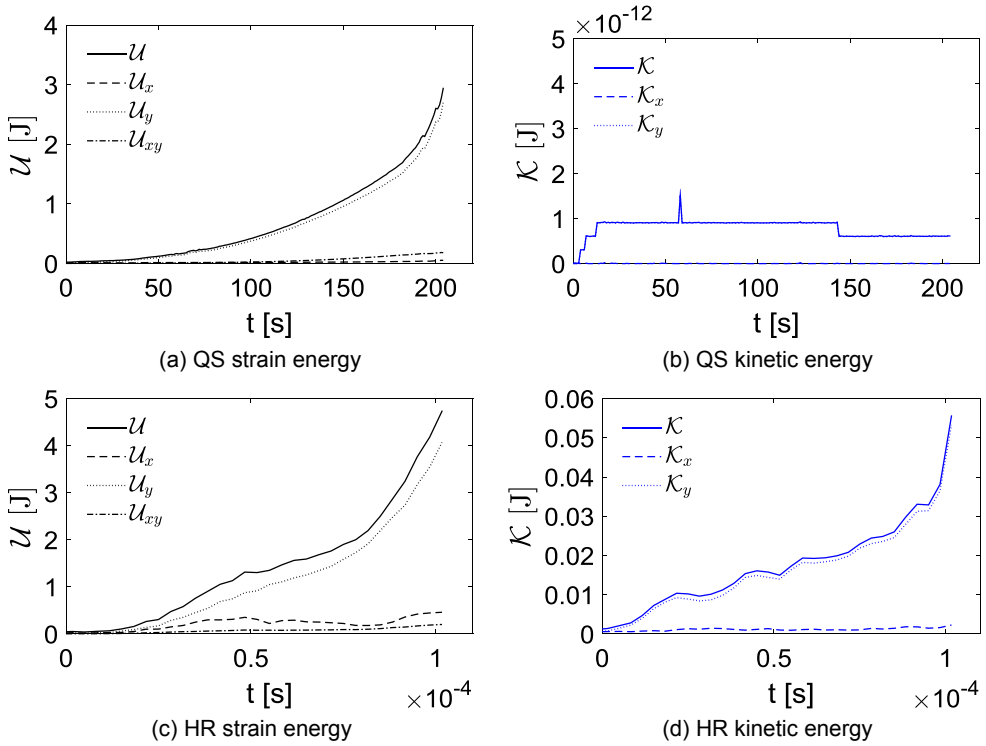

Figure 15: Example of strain and kinetic energy terms for QS (a, b) and HR (c, d) loading (specimen size D).

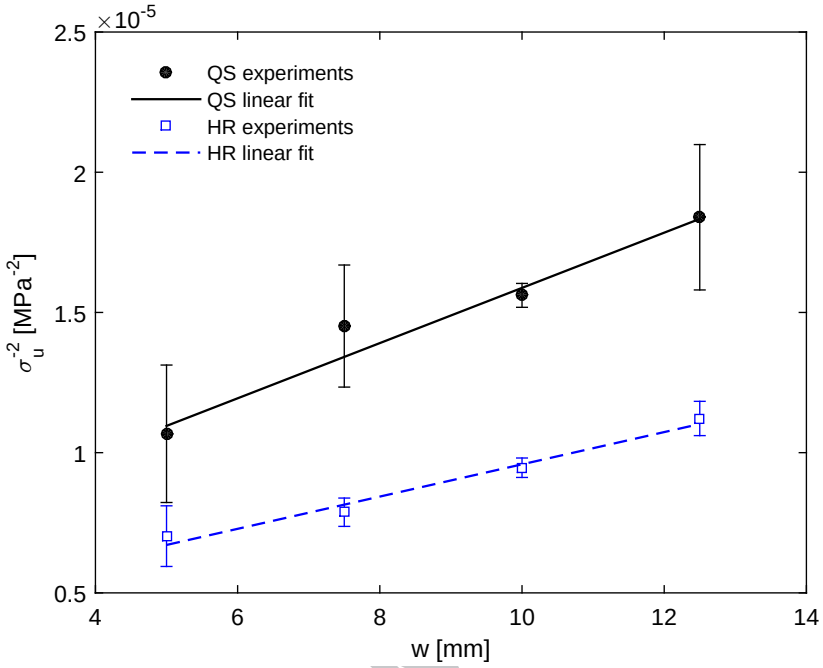

Figure 16: σ_u^{-2} vs. w and linear fitting for QS and HR loading.

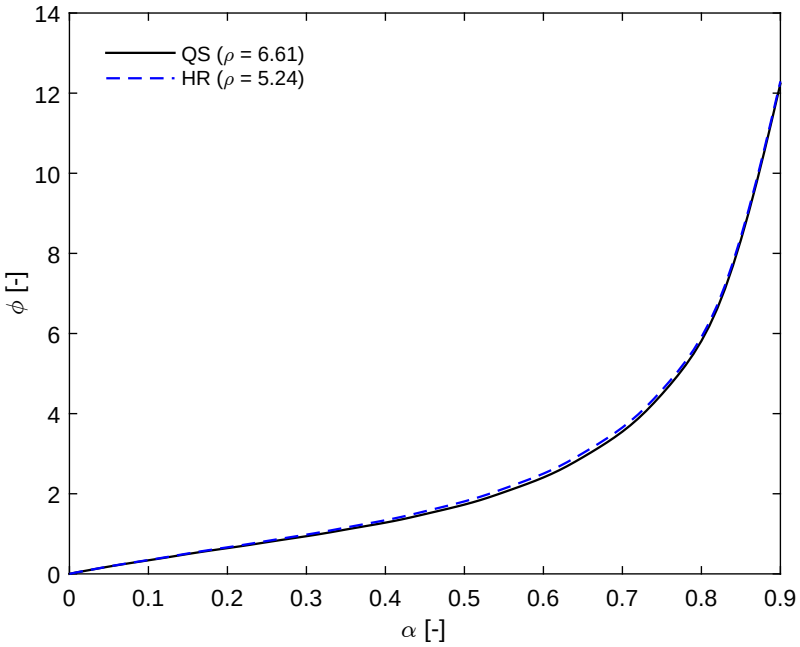

Figure 17: Correction function ϕ vs. specimen size w for QS and HR loading.

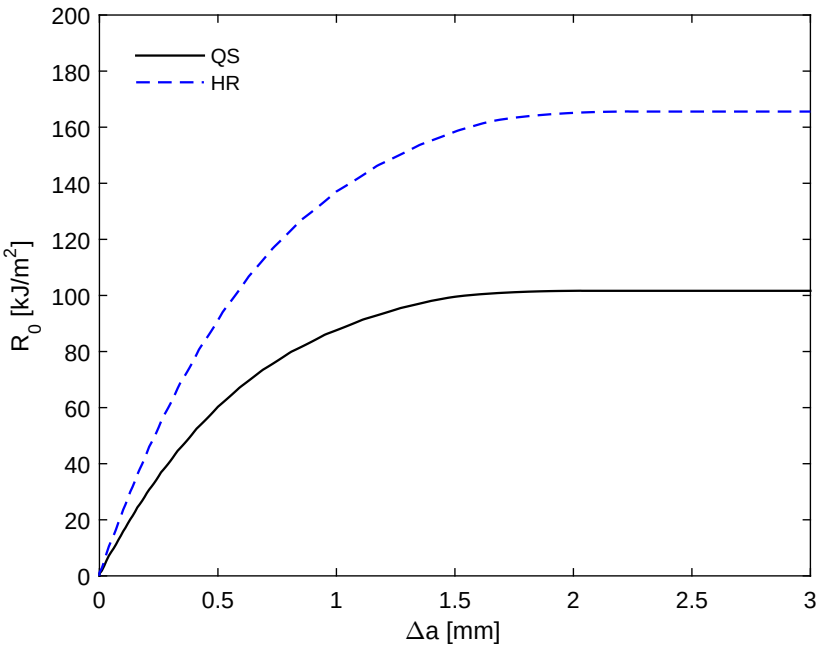

Figure 18: Compressive R-curve of IM7-8552 for QS and HR loading.

Figures Appendix A

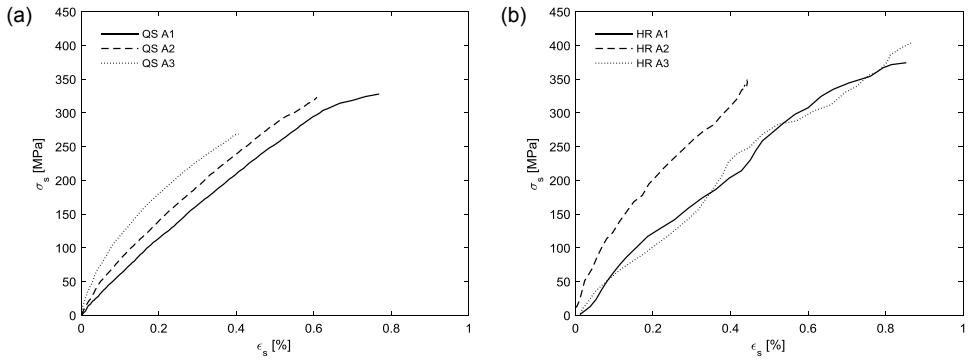

Figure A.1: Stress-strain responses of specimen size A for QS (a) and HR (b) loading.

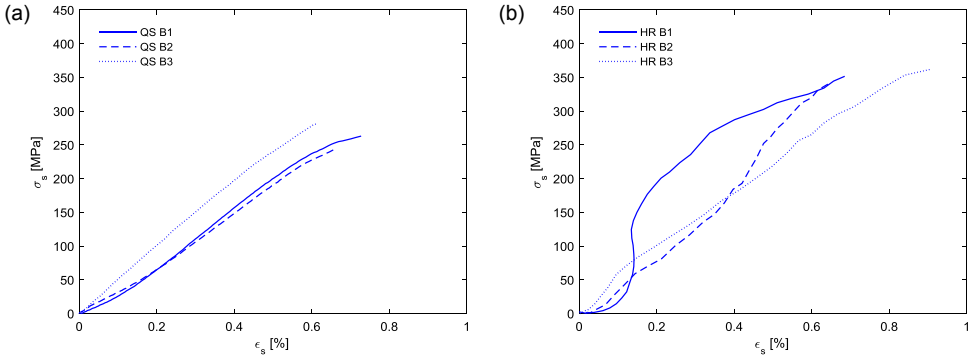

Figure A.2: Stress-strain responses of specimen size B for QS (a) and HR (b) loading.

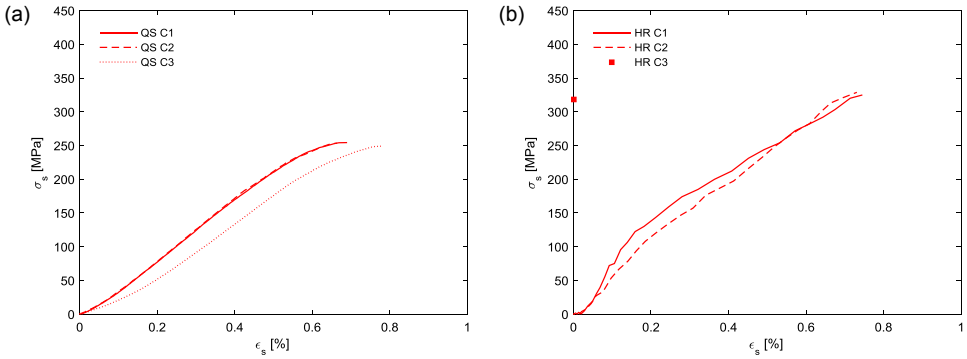

Figure A.3: Stress-strain responses of specimen size C for QS (a) and HR (b) loading.

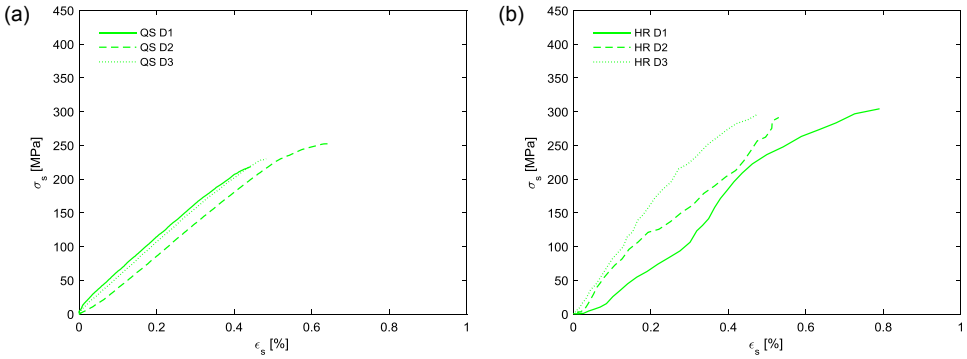

Figure A.4: Stress-strain responses of specimen size D for QS (a) and HR (b) loading.

Figures Appendix B

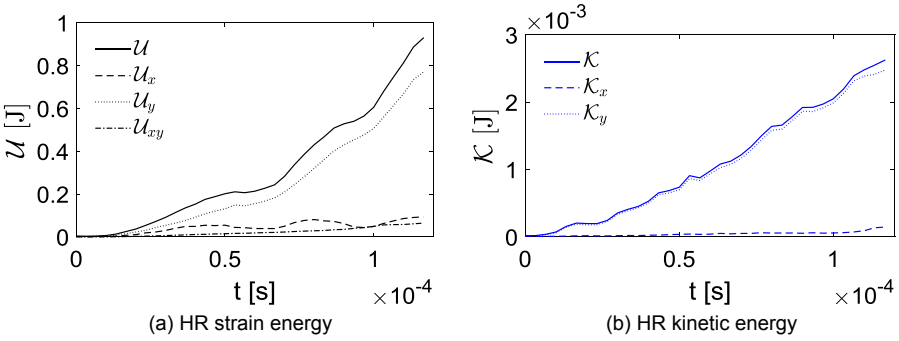

Figure B.1: Example of strain (a) and kinetic (b) energy terms for HR loading of specimen size A.

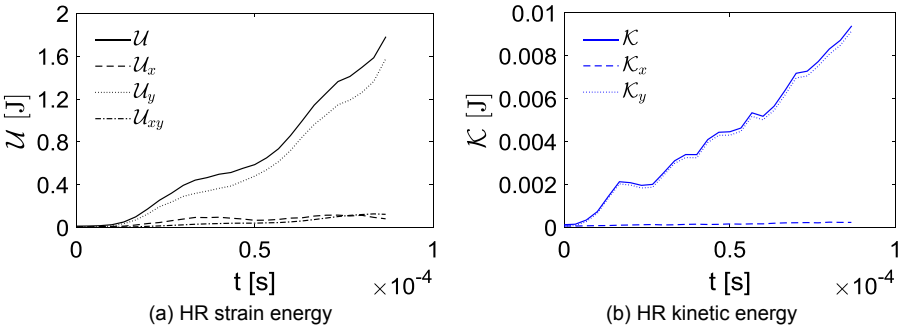

Figure B.2: Example of strain (a) and kinetic (b) energy terms for HR loading of specimen size B.

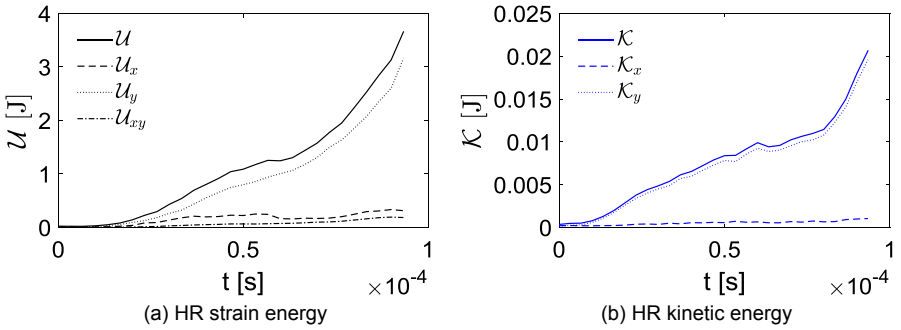

Figure B.3: Example of strain (a) and kinetic (b) energy terms for HR loading of specimen size C.

Tables

Table 1: Elastic properties of the laminate.

Strain rate regime	E [MPa]	G_{xy} [MPa]	ν_{xy} [-]	ρ [-]
QS	67,449	5,068	0.042	6.61
HR	67,126	6,345	0.048	5.24

Table 2: Split-Hopkinson pressure bar parameters.

Specimen type	w [mm]	d_b [mm]	v_s [m/s]	Pulse Shaper dimensions [mm]	
				d_{PS}	t_{PS}
A	5	16	8.6	6	1.5
B	7.5	18	9.4	8	1.5
C	10	18	11.0	10	2.0
D	12.5	25	12.2	10	2.0

Table 3: ARAMIS analysis parameters.

Parameter	QS	HR			
		A	B	C	D
Conversion factor [mm/pixel]	0.021	0.084	0.127	0.170	0.224
Facet size [pixel^2]	17 x 17	10 x 10			
Facet step [pixel^2]	15 x 15	5 x 5			
Computation size [facets^2]	5 x 5	5 x 5			

Table 4: Summary of the experimental results

		A	B	C	D
	w [mm]	5	7.5	10	12.5
QS	σ_u [MPa]	310	264	253	234
	STDV (σ_u) [MPa]	33	20	3	17
HR	σ_u [MPa]	380	357	325	299
	STDV (σ_u) [MPa]	29	11	6	8

Table 5: Linear curve fitting parameters.

Strain rate regime	m	q	R^2
	[MPa^{-2} mm^{-1}]	[MPa^{-2}]	[-]
QS	9.84×10^{-7}	6.03×10^{-6}	0.960
HR	5.75×10^{-7}	3.83×10^{-6}	0.982

Table 6: Summary of the fracture toughness properties.

Strain rate regime	R^0_{ss} [kJ/m^2]	l_{fpz} [mm]
QS	101.6	2.04
HR	165.6	2.24

Table 7: Fitting parameters of the analytical R-curves.

Strain rate regime	κ [mm^{-1}]	n [-]	R^2 [-]
QS	0.3794	4.247	0.9998
HR	0.3493	4.143	0.9998